STRUCTURAL CHEMISTRY

ISSN 2053-2296

Crystallographic and physicochemical characterization of salcaprozoic acid: a structural basis for SNAC-enabled drug delivery systems

Parag Roy,[a]* Paul G. Waddell,[b] Rajdeep Dey[c] and Oisín N. Kavanagh[a]*

[a]School of Pharmacy, Newcastle University, Newcastle upon Tyne, NE1 7RU, United Kingdom, [b]School of Natural and Environmental Sciences, Newcastle University, Newcastle upon Tyne, NE1 7RU, United Kingdom, and [c]Department of Pharmaceutical Chemistry, Institute of Pharmacy, Nirma University, Ahmedabad, 382 481, India. *Correspondence e-mail: parag.roy@newcastle.ac.uk, oisin.kavanagh@newcastle.ac.uk

Received 16 May 2025
Accepted 3 October 2025

Edited by I. Oswald, University of Strathclyde, United Kingdom

Keywords: salcaprozoic acid; salcaprozate sodium; SNAC; HNAC; crystal structure; drug delivery system; oral permeation enhancer.

CCDC reference: 2451829

Supporting information: this article has supporting information at journals.iucr.org/c

Salcaprozate sodium (SNAC) is a clinically approved oral permeation enhancer, notably used in the formulation of oral semaglutide. Despite its pharmaceutical importance, the crystallographic information of SNAC or its free acid form, salcaprozoic acid {systematic name: 8-[(2-hydroxyphenyl)formamido]octanoic acid, $C_{15}H_{21}NO_4$, denoted HNAC}, has not been reported previously. Here, we present the first crystallographic and physicochemical characterization of HNAC using single-crystal X-ray diffraction and complementary analytical techniques. The structure reveals the molecular conformation, hydrogen-bonding network and packing features of HNAC, supported by a complementary solid-state dataset. These findings provide fundamental insights into the structural and physicochemical properties of this physiologically relevant form of SNAC.

1. Introduction

Salcaprozate sodium ($Na^+ \cdot C_{15}H_{20}NO_4^-$, SNAC) is a synthetic derivative of salicylic acid, known as sodium 8-[(2-hydroxybenzoyl)amino]caprylate. It has drawn significant attention as a permeation enhancer to facilitate the oral administration of therapeutics, particularly for macromolecules that typically exhibit poor gastrointestinal absorption (Twarog *et al.*, 2019). The amphiphilic structure of SNAC facilitates transcellular drug transport by modulating the fluidity of the epithelial membrane and pH microenvironment at the site of absorption, thereby enhancing absorption of co-administered molecules without causing long-term mucosal damage (Kommineni *et al.*, 2023). SNAC has been used in formulations of drugs that have undergone clinical trials and has achieved Generally Recognized As Safe (GRAS) status, with US Food and Drug Administration (FDA) approval for use in medical and food products (Castelli *et al.*, 2011). The clinical significance of SNAC is exemplified by its incorporation into the oral formulation of semaglutide, a glucagon-like peptide-1 (GLP-1) receptor agonist (Solis-Herrera *et al.*, 2024). The key part of the mechanism of action of SNAC involves neutralizing the local pH in the stomach and initiating monomerization of the peptide, thereby stabilizing semaglutide and reducing its degradation. Under physiological conditions, SNAC could dissociate into its free acid form, salcaprozoic acid ($C_{15}H_{21}NO_4$, HNAC) and sodium ion components (Rebollo *et al.*, 2025).

Despite its extensive application in drug delivery systems, to the best of our knowledge, no reports of comprehensive crystallographic studies of SNAC or its free acid form HNAC,

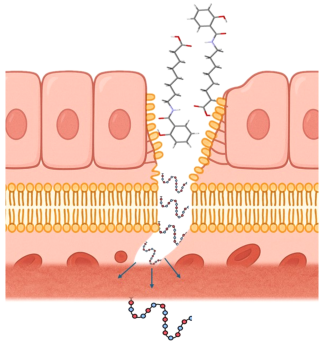

have been reported to date. Knowledge of the crystallographic information could be useful as the structural properties are directly relevant to its *in vivo* behaviour (Datta & Grant, 2004). A deeper understanding of the molecular conformation and interactions in the solid state can provide insights into the intrinsic physicochemical characteristics which could be beneficial for pharmaceutical development and mechanistic modelling of structurally related permeation enhancers.

In this study, we report the single-crystal X-ray structure of HNAC (Scheme 1), revealing its molecular conformation, hydrogen-bonding network and crystal packing features, along with other solid-state characterization studies. This represents the first crystallographic characterization of the free acid form and offers a structural basis for future investigations into medium-chain fatty-acid-related molecular systems. During our work, we also synthesized SNAC; however, despite multiple crystallization attempts, we were unable to obtain single crystals suitable for X-ray diffraction. This further underscores the significance of the present result, as it provides valuable structural insight into a key physiologically relevant form of this important permeation enhancer.

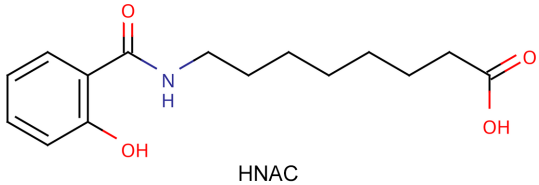

HNAC
Scheme 1

2. Experimental

2.1. Single-crystal X-ray diffraction (SCXRD) data collection and refinement

Details of the crystal structure refinement and refinement statistics for HNAC are given in Table 1. The sample of HNAC (≥98% purity) was procured from Synlyfe Research Laboratory (Gujarat, India). Crystals of HNAC were obtained by slow evaporation of a methanolic solution at room temperature (≃ 298 K). A 5 ml sample of the compound dissolved in methanol was left undisturbed, and solvent evaporation over a period of 5–6 d yielded crystals suitable for analysis.

H atoms were positioned with idealized geometry, with the exception of those bound to heteroatoms, the positions of which were located using peaks in the Fourier difference map, with their coordinates allowed to refine freely. The displacement parameters of the H atoms, U_{iso}, were constrained using a riding model, with U_{iso}(H) set to be an appropriate multiple of the U_{eq} value of the parent atom.

2.2. Powder X-ray diffraction

Powder X-ray diffraction patterns were recorded using an Empyrean diffractometer (Malvern Panalytical, UK) in Bragg–Brentano θ/θ geometry, equipped with a PIXcel 3D detector and a reflection–transmission spinner stage. The instrument utilized monochromatic Cu $K\alpha_1$ radiation (λ = 1.54184 Å) generated at 40 kV and 40 mA, with a take-off angle of 6.0°. Data were collected at room temperature over a 2θ range of 5 to 40°, with a step size of 0.01° and 20 s per step. The obtained diffractograms were analyzed using *HighScore Plus* (Malvern Panalytical, UK) software (Degen *et al.*, 2014). Rietveld refinement was performed using the structural model derived from single-crystal data, allowing accurate determination of lattice parameters, phase identification and confirmation of the sample purity.

Table 1
Experimental details.

Crystal data	
Chemical formula	$C_{15}H_{21}NO_4$
M_r	279.33
Crystal system, space group	Monoclinic, $P2_1/c$
Temperature (K)	150
a, b, c (Å)	10.1779 (2), 23.7511 (6), 11.8738 (3)
β (°)	101.124 (2)
V (Å^3)	2816.40 (12)
Z	8
Radiation type	Cu $K\alpha$
μ (mm^{-1})	0.78
Crystal size (mm)	0.19 × 0.04 × 0.02
Data collection	
Diffractometer	Rigaku OD XtaLAB Synergy-S HyPix-Arc 100
Absorption correction	Analytical [*CrysAlis PRO* (Rigaku OD, 2024) based on expressions derived by Clark & Reid (1995)]
T_{min}, T_{max}	0.922, 0.989
No. of measured, independent and observed [$I > 2\sigma(I)$] reflections	21630, 5561, 4555
R_{int}	0.036
(sin $\theta/\lambda)_{max}$ (Å^{-1})	0.633
Refinement	
$R[F^2 > 2\sigma(F^2)]$, $wR(F^2)$, S	0.046, 0.131, 1.06
No. of reflections	5561
No. of parameters	379
H-atom treatment	H atoms treated by a mixture of independent and constrained refinement
$\Delta\rho_{max}$, $\Delta\rho_{min}$ (e Å^{-3})	0.31, −0.18

Computer programs: *CrysAlis PRO* (Rigaku OD, 2024), *SHELXT2018* (Sheldrick, 2015), *SHELXL* (Sheldrick, 2008) and *OLEX2* (Dolomanov *et al.*, 2009).

2.3. Thermal analysis

Differential scanning calorimetry (DSC) was carried out using a TA Instruments Q2000 system (Cheshire, UK) over a temperature range of 30–300 °C. Approximately 2–5 mg of each sample were weighed into hermetically sealed aluminium pans and heated at a rate of 10 °C min^{-1} under a constant nitrogen purge (50 ml min^{-1}) to prevent oxidative degradation. The resulting thermograms were analysed using TA Instruments *Universal Analysis* software (https://www.tainstruments.com/).

Thermogravimetric analysis (TGA) was also performed to assess the decomposition behaviour of the samples. Measurements were conducted under a nitrogen atmosphere using a TA Instruments Q500 system (Cheshire, UK). 2–5 mg of samples were weighed into aluminium pans and heated from 30 to 500 °C at a constant heating rate of 10 °C min^{-1}. The

Table 2
Hydrogen-bond geometry (Å, °).

D—H···A	D—H	H···A	D···A	D—H···A
O1—H1···O2	0.89 (2)	1.76 (2)	2.5737 (16)	151 (2)
O4—H4···O2^{i}	0.93 (2)	1.73 (2)	2.6637 (15)	177 (2)
O5—H5A···O6	0.87 (2)	1.76 (2)	2.5660 (15)	153.1 (19)
O8—H8···O6^{ii}	0.94 (2)	1.71 (2)	2.6479 (15)	176.4 (19)
N1—H1A···O7	0.887 (19)	2.15 (2)	3.0220 (17)	169.3 (17)
N2—H2···O3	0.905 (19)	2.078 (19)	2.9708 (17)	168.6 (16)

Symmetry codes: (i) $-x+2, y-\frac{1}{2}, -z+\frac{1}{2}$; (ii) $-x+1, y+\frac{1}{2}, -z+\frac{3}{2}$.

resulting thermograms were analysed using TA Instruments *Universal Analysis* software.

2.4. Fourier–transform IR spectroscopy

IR spectra were recorded using an Agilent Cary 630 FT–IR spectrometer equipped with a diamond attenuated total reflectance (ATR) accessory. The instrument was operated with *MicroLab* FT–IR software (https://www.agilent.com/en/product/molecular-spectroscopy/ftir-spectroscopy) for spectral acquisition and processed by *OriginPro* software (OriginLab Corporation, 2022). Samples were analysed in their solid form without further preparation. Each spectrum was obtained over the range 4000–650 cm^{-1}. The obtained spectra were processed to identify characteristic functional group vibrations.

2.5. Synthesis of SNAC

HNAC (100 mg) was transferred to a 25 ml round-bottomed flask equipped with a magnetic stirrer bar. Isopropanol (≥99.5% purity, 5.0 ml) was added and the mixture was heated to 50 °C with constant stirring until a clear solution was obtained. An aqueous solution of sodium hydroxide (1 *M*) was added dropwise over a period of 5 min under continuous stirring until the pH reached 9–10, at which point a white precipitate of SNAC began to form. The reaction mixture was stirred at room temperature for an additional 30 min, and the precipitate was collected by vacuum filtration and dried at ambient temperature. PXRD (Fig. S1 in the supporting information) and DSC analysis confirmed the material as polymorphic form II (Levchik *et al.*, 2016). However, despite multiple crystallization attempts from various solvent systems, we were unable to obtain single crystals suitable for X-ray diffraction analysis.

3. Results and discussion

3.1. Cystal structure analysis

HNAC crystallizes in the monoclinic space group $P2_1/c$ (Fig. 1), with two crystallographically independent molecules in the asymmetric unit ($Z' = 2$) that are related by approximate inversion symmetry. Overlaying the two molecules further demonstrates this relationship, revealing two distinct conformations.

The asymmetric unit is held together by hydrogen bonds (Table 2) in which the amide proton donates to the carbonyl O atom of the carboxylic acid group to form a ring motif with the graph set $R_2^2(22)$ (Etter, 1990). These rings are linked by further hydrogen bonds, where the carboxylic acid group acts as a donor to the carbonyl O atom of the amide, forming a 2D network coplanar with the crystallographic (101) plane (Fig. 2). There do not appear to be any salient intermolecular interactions between these hydrogen-bonded layers.

In addition, an intramolecular hydrogen bond forms between the hydroxyl group and the amide carbonyl group, as would be anticipated according to Etter's second rule of hydrogen bonding (Etter, 1990).

In the absence of an experimentally resolved structure for SNAC, despite several attempts, the structure of HNAC can instead be compared with known examples in the Cambridge Structural Database (CSD; Groom *et al.*, 2016) that share similar fragments and functionalities. The structures of other medium-chain fatty acids which acts as permeation enhancers like heptanoic acid (Bond, 2004; CSD refcode ISENOJ) and suberic acid (Mishra *et al.*, 2015; SUBRAC12) exhibit the same antiperiplanar arrangement along the length of the carbon

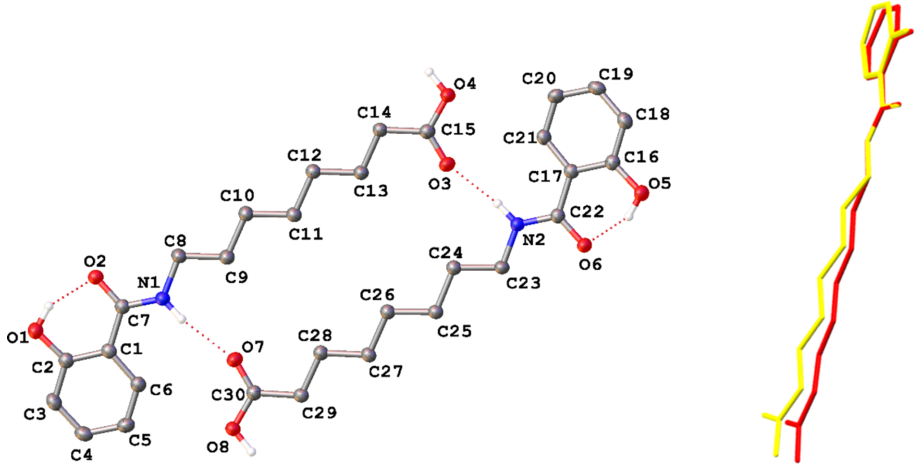

Figure 1
The asymmetric unit of HNAC, with selected atom labelling, showing (left) displacement ellipsoids plotted at the 50% probability level and (right) an overlay of the two symmetry-independent molecules. H atoms bound to C atoms have been omitted for clarity.

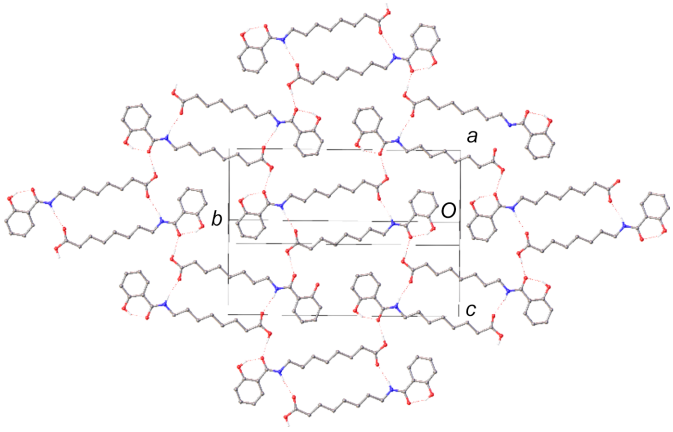

Figure 2
The 2D hydrogen-bonded layer in the (101) plane of the crystal structure of HNAC. H atoms bound to C atoms have been omitted for clarity.

chain as that observed in HNAC, though in these instances hydrogen bonding is observed between carboxylic acid groups forming $R_2^2(22)$ ring motifs. This is likely attributable to the absence of alternative donor or acceptor sites in these structures, unlike in HNAC, where multiple options are available.

In terms of the 2-hydroxybenzoylamino moiety, few examples are available that possess a similar saturated carbon chain with terminal hydrogen-bond donors or acceptors, with the closest being 2-hydroxy-*N*-(2-hydroxyethyl)benzamide (CSD refcode family EVIWIQ). Among the two available examples of this structure in the CSD (Betz *et al.*, 2011; Wanke *et al.*, 2011), the entry EVIWIQ01 reported by Wanke and co-authors was selected for comparison, as its data were collected at the same temperature as HNAC (150 K).

Considering the structural fragment that both HNAC and EVIWIQ01 share, the two exhibit relatively similar conformations (Fig. 3). Where they do differ is in the orientation of the benzene ring relative to the amide moiety. Where in HNAC the N1—C7—C1—C6 torsion angles are 4.43 (15) and 6.45 (15)°, the equivalent torsion in EVIWIQ01 is 12.2 (2)°, representing a significant deviation from planarity.

This can be rationalized by considering the relative directions of the hydrogen bonds in each structure. In HNAC, the bonds are all essentially in the plane of the hydrogen-bonding network [*i.e.* the (101) plane]. However, in EVIWIQ01, though the structure ultimately forms a 2D network in the (100) plane, the hydrogen bonds are not in this plane (*e.g.* O3—H4···O2 forms an angle of *ca* 22° with the *b* axis). These attractive forces therefore act at an angle to the plane of the molecule and lead to greater distortions of the otherwise planar geometry. The absence of similar interactions in HNAC allows it to form the almost perfectly planar sheets observed in the structure.

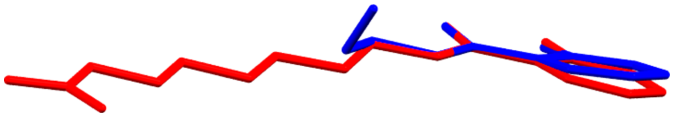

Figure 3
An overlay of one of the independent molecules of HNAC (red) and that of EVIWIQ01 (blue). H atoms have been omitted for clarity.

3.2. Powder X-ray diffraction and Rietveld refinement

The crystalline structure of HNAC was confirmed by Rietveld refinement of the PXRD data using *HighScore Plus* (Fig. 4). The experimental diffraction pattern was measured using monochromatic Cu $K\alpha_1$ radiation (λ = 1.54184 Å) and refinement was performed against the single-phase structural model derived from the CIF. Closer inspection of the diffraction profile revealed weak shoulder features, notably near 7.5° 2θ. These could be accounted for within the Rietveld model as overlapping reflections from the same monoclinic phase, combined with low-angle axial divergence effects. The refinement converged successfully with good agreement between the calculated and experimental patterns. The goodness-of-fit (GoF) was 2.541, with the weighted profile *R* factor (R_{wp}) = 6.295%, profile *R* factor (R_p) = 4.708% and Bragg *R* factor = 2.001%. The expected *R* factor was 2.477%, indicating a well-fitted model with no overfitting. All Bragg reflections could be indexed to a single monoclinic phase, $P2_1/c$, and no additional peaks were detected. The refined unit-cell parameters from the PXRD data (a = 10.23430, b = 23.73930, c = 12.04533 Å and β = 100.0874°) closely match those from the SCXRD data. The Rietveld refinement confirms that the sample is crystalline and structurally consistent with the reference CIF which supports the

Figure 4
Rietveld refinement of the PXRD pattern of HNAC. Colour code: red = observed data; blue = calculated profile; purple = difference plot; green vertical tick marks = Bragg reflection positions.

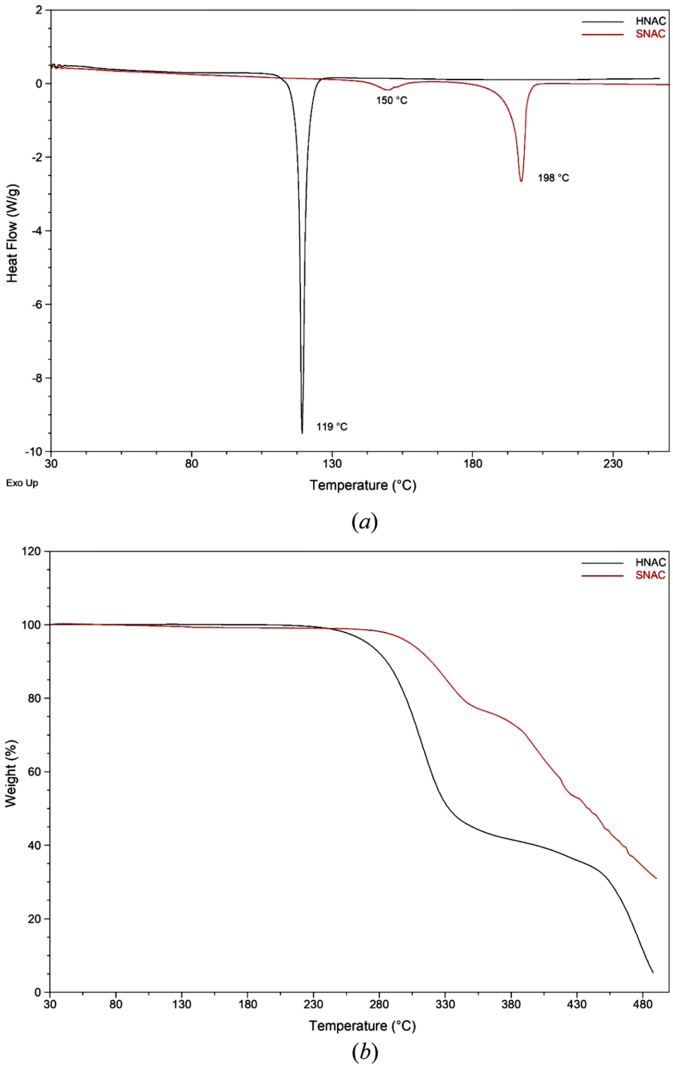

Figure 5
Combined (*a*) DSC thermogram and (*b*) TGA endotherm of HNAC.

reasoning that the shoulders arise from intrinsic profile broadening rather than from impurities or an additional polymorph.

3.3. Thermal analysis

The thermal behaviours of HNAC and SNAC were investigated by DSC and TGA (Fig. 5). HNAC exhibits a single sharp endotherm at approximately 119 °C, indicative of the melting point, which is consistent with the existing literature reports (Rebollo *et al.*, 2025). The TGA curve of HNAC shows a rapid and substantial weight loss immediately following melting, suggesting that decomposition is triggered directly after the phase transition. SNAC demonstrates a minor endothermic peak at approximately 150 °C and a sharp endothermic peak at approximately 198 °C, characteristic of polymorphic form II (Levchik *et al.*, 2016). The TGA profile confirms that SNAC undergoes a two-stage decomposition process, with initial mass loss beginning after 198 °C, followed by progressive degradation at higher temperatures. The thermal profiles are consistent with the molecular structures of the HNAC and SNAC. For HNAC, the neutral carboxylic acid form, melting at 119 °C, appears to assist rapid volatilization and breakdown of the molecular framework, possibly through decarboxylation and cleavage of the amide linkage. Whereas the ionic stabilization of the carboxylate group of SNAC delays the decomposition to higher temperatures. The stepwise mass losses observed for SNAC suggest that the initial stage may involve fragmentation of more labile substituents, followed by degradation of the aliphatic chain and aromatic core.

3.4. IR spectroscopy

The IR spectra of HNAC and SNAC provide valuable insights into the structural and electronic differences induced by deprotonation and salt formation. These changes are particularly evident in the regions corresponding to O—H, C═O, C—N and aromatic functionalities.

In the IR spectrum of HNAC (Fig. 6), a broad and intense band centred around 3352 cm^{-1} is attributed to the O—H stretching vibration of the carboxylic acid group (Shen *et al.*, 2024). This broadness is indicative of strong hydrogen bonding, which is characteristic of carboxylic acids (Langner & Zundel, 1995). Additionally, the phenolic –OH group may also contribute to this band, but its involvement in intermolecular hydrogen bonding with neighbouring molecules could influence its precise position and intensity (Yamashita & Takatsuka, 2007). Upon the formation of the sodium salt, SNAC, the O—H stretching band is significantly diminished or absent, indicating deprotonation of the carboxylic acid and the formation of the carboxylate anion (COO^-). The disappearance of this peak is consistent with ionic salt formation, where the H atom is replaced by a sodium ion (Na^+), resulting in altered vibrational characteristics. Moreover, the phenolic –OH group may undergo extensive intermolecular hydrogen bonding, especially in the solid state, which can either shift the absorption to lower frequencies or render it IR-inactive due to reduced dipole change during vibration (Dai *et al.*, 2023).

The C═O stretching vibration is another critical diagnostic region. In the free acid, a strong sharp absorption at 1727 cm^{-1} corresponds to the carbonyl (C═O) stretch of the carboxylic acid group. This peak is notably absent or shifted in the SNAC spectrum. Instead, a prominent band appears around 1589 cm^{-1}, which is characteristic of the asymmetric stretching of the carboxylate anion (COO^-) (Max & Chapados, 2004). This shift to lower wavenumbers reflects the delocalization of negative charge across the two O atoms in the carboxylate group, reducing the bond order and thus lowering the stretching frequency (Dey *et al.*, 2025). Additionally, the amide functional group is evident in both spectra. The amide II band, arising from N—H bending coupled with C—N stretching, is observed in the range 1597–1554 cm^{-1}. Hydrogen bonding or conjugation with the aromatic ring may influence the exact position and intensity of this band. The C—N stretching vibration of the amide is detected near 1299 cm^{-1}, further confirming the presence of the amide moiety.

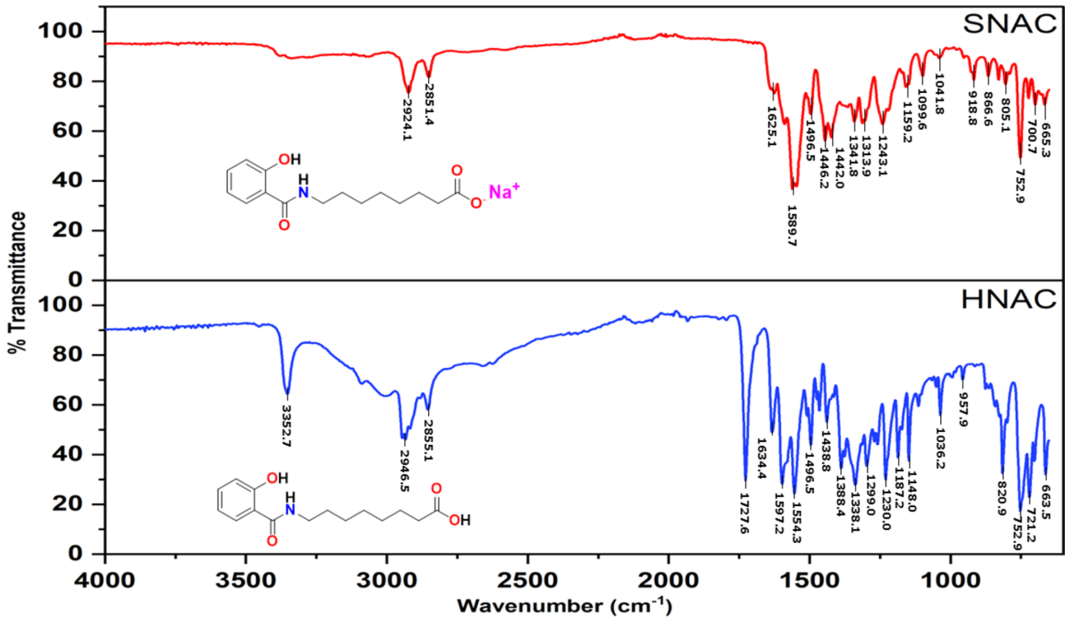

Figure 6
FT–IR spectra of HNAC and SNAC.

Aromatic features are clearly present in both spectra. The C═C stretching vibrations of the aromatic ring are observed as multiple medium-intensity bands in the range 1450–1600 cm^{-1}, consistent with a substituted benzene ring system. The C—O stretching vibrations, arising from both phenolic and carboxylic acid groups, occur near 1230 cm^{-1}, although these can sometimes overlap with C—N stretches depending on the local environment and substitution pattern. The aliphatic C—H stretching vibrations are represented by strong bands around 2945 and 2924 cm^{-1}, common to both the acid and salt forms. These arise from the symmetric and asymmetric stretching modes of CH_2 groups in the aliphatic chain. Furthermore, aromatic C—H out-of-plane bending vibrations appear around 870 cm^{-1}, supporting the presence of mono- or disubstituted benzene rings, which are key structural motifs in HNAC and SNAC (Lin-Vien *et al.*, 1991).

4. Conclusions

This study presents the first comprehensive crystallographic characterization of salcaprozoic acid (HNAC), the free acid form of salcaprozate sodium (SNAC), using single-crystal X-ray diffraction. The results show that HNAC crystallizes in the monoclinic space group $P2_1/c$, with two molecules in the asymmetric unit, stabilized by an extensive network of intra- and intermolecular hydrogen bonds. This well-organized hydrogen-bonding framework underpins the robust crystal packing and thermal stability of the compound, as further corroborated by thermal analysis and powder X-ray diffraction. Complementary IR spectroscopy confirmed the presence of key functional groups and highlighted the impact of hydrogen bonding on vibrational modes.

Placing these findings in the broader context of lipid-based permeation enhancers, HNAC retains structural features typical of other medium-chain fatty acids, such as extended aliphatic chain conformations, while also introducing an additional aromatic amide fragment. This distinguishes HNAC from other medium-chain fatty acids which act as permeation enhancers, like heptanoic acid and suberic acid. Crystallographically, this study shows the difference between simpler and more complex lipid-based permeation enhancers. The insights into the molecular conformation and solid-state interactions of HNAC could enhance our understanding of its physicochemical properties, providing a valuable structural foundation for the development and optimization of SNAC-based drug delivery systems and related permeation enhancers.

Acknowledgements

OK is supported by Action Medical Research/LifeArc funding. OK and PR are supported by an Engineering and Physical Sciences Research Council grant. The authors also thank Tanzeela Anis for helpful discussions about Rietveld refinement.

Funding information

Funding for this research was provided by: Action Medical Research/LifeArc (grant No. GN3039 to O. N. Kavanagh); Engineering and Physical Sciences Research Council (grant No. EP/Y014596/1 to O. N. Kavanagh and P. Roy).

References

Betz, R., Gerber, T., Hosten, E. & Schalekamp, H. (2011). *Acta Cryst.* E**67**, o2117.
Bond, A. D. (2004). *New J. Chem.* **28**, 104–114.

Castelli, M. C., Wong, D. F., Friedman, K. & Riley, M. G. I. (2011). *Clin. Ther.* **33**, 934–945.
Clark, R. C. & Reid, J. S. (1995). *Acta Cryst.* A**51**, 887–897.
Dai, F., Zhuang, Q., Huang, G., Deng, H. & Zhang, X. (2023). *ACS Omega* **8**, 17064–17076.
Datta, S. & Grant, D. J. (2004). *Nat. Rev. Drug Discov.* **3**, 42–57.
Degen, T., Sadki, M., Bron, E., König, U. & Nénert, G. (2014). *Powder Diffr.* **29**, S13–S18.
Dey, R., Shaw, S., Yadav, R., Patel, B. D., Bhatt, H. G., Natesan, G., Jha, A. B. & Chaube, U. (2025). *Cancers* **17**, 759.
Dolomanov, O. V., Bourhis, L. J., Gildea, R. J., Howard, J. A. K. & Puschmann, H. (2009). *J. Appl. Cryst.* **42**, 339–341.
Etter, M. C. (1990). *Acc. Chem. Res.* **23**, 120–126.
Groom, C. R., Bruno, I. J., Lightfoot, M. P. & Ward, S. C. (2016). *Acta Cryst.* B**72**, 171–179.
Kommineni, N., Sainaga Jyothi, V. G., Butreddy, A., Raju, S., Shapira, T., Khan, W., Angsantikul, P. & Domb, A. J. (2023). *Pharm. Res.* **40**, 633–650.
Langner, R. & Zundel, G. (1995). *J. Chem. Soc. Faraday Trans.* **91**, 3831–3838.
Levchik, H., Majuru, S., Singh, B. & Harris, J. (2016). US Patent US20160184251A1. https://patents.google.com/patent/US20160184251A1/zh-TW.
Lin-Vien, D., Colthup, N. B., Fateley, W. G. & Grasselli, J. G. (1991). In *The handbook of infrared and raman characteristic frequencies of organic molecules.* San Diego: Academic Press.
Max, J.-J. & Chapados, C. (2004). *J. Phys. Chem. A* **108**, 3324–3337.
Mishra, M. K., Ramamurty, U. & Desiraju, G. R. (2015). *Chem. Asian J.* **10**, 2176–2181.
OriginLab Corporation (2022). *OriginPro*. OriginLab Corporation, Northampton, MA, USA. https://www.originlab.com/.
Rebollo, R., Niu, Z., Blaabjerg, L., La Zara, D., Juel, T., Pedersen, H. D., Andersson, V., Benova, M., Krogh, C., Pons, R., Holm, T. P., Wahlund, P. O., Fan, L., Wang, Z., Kennedy, A., Kuhre, R. E., Christophersen, P., Bardonnet, P. L. & Sassene, P. J. (2025). *J. Control. Release* **377**, 267–276.
Rigaku OD (2024). *CrysAlis PRO*. Rigaku Oxford Diffraction Ltd, Yarnton, Oxfordshire, England.
Sheldrick, G. M. (2008). *Acta Cryst.* A**64**, 112–122.
Sheldrick, G. M. (2015). *Acta Cryst.* A**71**, 3–8.
Shen, Z., Chen, J., Ge, J., Cai, Z., Hua, X.-N. & Sun, B. (2024). *Struct. Chem.* **35**, 967–975.
Solis-Herrera, C., Kane, M. P. & Triplitt, C. (2024). *Clin. Diabetes* **42**, 74–86.
Twarog, C., Fattah, S., Heade, J., Maher, S., Fattal, E. & Brayden, D. J. (2019). *Pharmaceutics* **11**, 78.
Wanke, R., Benisvy, L., Kuznetsov, M. L., Guedes da Silva, M. F. C. & Pombeiro, A. J. L. (2011). *Chem. A Eur. J.* **17**, 11882–11892.
Yamashita, T. & Takatsuka, K. (2007). *J. Chem. Phys.* **126**, 074304.

supporting information

Acta Cryst. (2025). C**81**, 607-613 [https://doi.org/10.1107/S2053229625008691]

Crystallographic and physicochemical characterization of salcaprozoic acid: a structural basis for SNAC-enabled drug delivery systems

Parag Roy, Paul G. Waddell, Rajdeep Dey and Oisín N. Kavanagh

Computing details

8-[(2-Hydroxyphenyl)formamido]octanoic acid

Crystal data

$C_{15}H_{21}NO_4$
M_r = 279.33
Monoclinic, $P2_1/c$
a = 10.1779 (2) Å
b = 23.7511 (6) Å
c = 11.8738 (3) Å
β = 101.124 (2)°
V = 2816.40 (12) Å^3
Z = 8
$F(000)$ = 1200
D_x = 1.318 Mg m^{-3}
Cu $K\alpha$ radiation, λ = 1.54184 Å
Cell parameters from 7874 reflections
θ = 3.7–76.7°
μ = 0.78 mm^{-1}
T = 150 K
Needle, colourless
0.19 × 0.04 × 0.02 mm

Data collection

Rigaku OD XtaLAB Synergy-S HyPix-Arc 100 diffractometer
Detector resolution: 10.0000 pixels mm^{-1}
Absorption correction: analytical [CrysAlis PRO (Rigaku OD, 2024) based on expressions derived by Clark & Reid (1995)]
T_{min} = 0.922, T_{max} = 0.989
21630 measured reflections
5561 independent reflections
4555 reflections with $I > 2\sigma(I)$
R_{int} = 0.036
θ_{max} = 77.2°, θ_{min} = 3.7°
h = −10→12
k = −28→28
l = −15→14

Refinement

Refinement on F^2
Least-squares matrix: full
$R[F^2 > 2\sigma(F^2)]$ = 0.046
$wR(F^2)$ = 0.131
S = 1.06
5561 reflections
379 parameters
0 restraints
Hydrogen site location: mixed
H atoms treated by a mixture of independent and constrained refinement
$w = 1/[\sigma^2(F_o^2) + (0.0695P)^2 + 0.6094P]$ where $P = (F_o^2 + 2F_c^2)/3$
$(\Delta/\sigma)_{max}$ = 0.001
$\Delta\rho_{max}$ = 0.31 e Å^{-3}
$\Delta\rho_{min}$ = −0.18 e Å^{-3}

Special details

Geometry. All esds (except the esd in the dihedral angle between two l.s. planes) are estimated using the full covariance matrix. The cell esds are taken into account individually in the estimation of esds in distances, angles and torsion angles; correlations between esds in cell parameters are only used when they are defined by crystal symmetry. An approximate (isotropic) treatment of cell esds is used for estimating esds involving l.s. planes.

Refinement. Single-crystal diffraction on an XtaLAB Synergy-S HyPix-Arc 100 diffractometer using copper radiation (λ = 1.54184 Å) at 150 K using an Oxford Cryosystems CryostreamPlus open-flow N_2 cooling device. Intensities were corrected for absorption using a multifaceted crystal model created by indexing the faces of the crystal for which data were collected (Clark & Reid, 1995). Unit-cell refinement, data collection and data reduction were undertaken *via* the software *CrysAlis PRO*.
The structure was solved using *SHELXT* (Sheldrick, 2015*a*) and refined by *SHELXL* (Sheldrick, 2008) using the *OLEX2* interface (Dolomanov *et al.*, 2009).

Fractional atomic coordinates and isotropic or equivalent isotropic displacement parameters (Å²)

	x	*y*	*z*	U_{iso}*/U_{eq}
O1	0.83294 (12)	0.94943 (5)	0.42674 (11)	0.0409 (3)
H1	0.8685 (19)	0.9208 (10)	0.3941 (18)	0.049*
O2	0.88203 (11)	0.84827 (4)	0.36903 (9)	0.0330 (3)
O3	0.82809 (12)	0.35069 (5)	0.38386 (11)	0.0430 (3)
O4	0.95540 (12)	0.31646 (5)	0.27015 (11)	0.0394 (3)
H4	1.0131 (19)	0.3286 (9)	0.2232 (18)	0.047*
O5	0.69882 (12)	0.11260 (5)	0.59731 (10)	0.0363 (3)
H5A	0.6568 (19)	0.1409 (9)	0.6217 (18)	0.044*
O6	0.61606 (11)	0.21249 (4)	0.62766 (10)	0.0360 (3)
O7	0.65798 (13)	0.70936 (5)	0.61018 (11)	0.0439 (3)
O8	0.53463 (12)	0.74468 (5)	0.72543 (10)	0.0372 (3)
H8	0.4793 (18)	0.7323 (9)	0.7752 (17)	0.045*
N1	0.80330 (13)	0.77318 (5)	0.45107 (12)	0.0311 (3)
H1A	0.7557 (18)	0.7588 (8)	0.4993 (16)	0.037*
N2	0.69399 (12)	0.28785 (5)	0.54628 (11)	0.0287 (3)
H2	0.7437 (17)	0.3032 (8)	0.4987 (16)	0.034*
C1	0.73861 (14)	0.86679 (6)	0.50076 (12)	0.0268 (3)
C2	0.75042 (14)	0.92546 (6)	0.49008 (13)	0.0294 (3)
C3	0.67538 (16)	0.96151 (7)	0.54537 (15)	0.0364 (4)
H3	0.683211	1.001118	0.537670	0.044*
C4	0.58986 (16)	0.93980 (7)	0.61118 (14)	0.0364 (4)
H4A	0.538714	0.964649	0.648321	0.044*
C5	0.57747 (16)	0.88216 (7)	0.62389 (14)	0.0363 (4)
H5	0.519086	0.867519	0.670206	0.044*
C6	0.65048 (15)	0.84637 (7)	0.56886 (13)	0.0319 (3)
H6	0.641116	0.806866	0.577068	0.038*
C7	0.81341 (14)	0.82827 (6)	0.43722 (12)	0.0272 (3)
C8	0.86912 (16)	0.73197 (6)	0.38917 (15)	0.0331 (3)
H8A	0.967436	0.734718	0.414539	0.040*
H8B	0.847093	0.739949	0.305816	0.040*
C9	0.82273 (16)	0.67297 (6)	0.41206 (14)	0.0326 (3)
H9A	0.724883	0.670211	0.383663	0.039*
H9B	0.840279	0.666230	0.495904	0.039*
C10	0.89268 (15)	0.62762 (6)	0.35457 (14)	0.0304 (3)
H10A	0.990576	0.630723	0.382339	0.037*
H10B	0.874364	0.634214	0.270668	0.037*
C11	0.84786 (15)	0.56826 (6)	0.37804 (13)	0.0300 (3)

H11A	0.750320	0.564930	0.348615	0.036*
H11B	0.864104	0.562044	0.462036	0.036*
C12	0.92001 (15)	0.52252 (6)	0.32301 (13)	0.0295 (3)
H12A	0.905038	0.529046	0.239153	0.035*
H12B	1.017429	0.525363	0.353458	0.035*
C13	0.87310 (15)	0.46357 (6)	0.34514 (14)	0.0311 (3)
H13A	0.776488	0.460220	0.311735	0.037*
H13B	0.884471	0.457622	0.428982	0.037*
C14	0.94929 (15)	0.41784 (6)	0.29439 (13)	0.0294 (3)
H14A	0.935330	0.422935	0.210172	0.035*
H14B	1.046245	0.421942	0.325763	0.035*
C15	0.90548 (15)	0.35954 (7)	0.32012 (14)	0.0322 (3)
C16	0.75655 (14)	0.19405 (6)	0.49337 (12)	0.0272 (3)
C17	0.76101 (14)	0.13589 (6)	0.51738 (13)	0.0292 (3)
C18	0.83324 (15)	0.09999 (7)	0.45916 (14)	0.0331 (3)
H18	0.836805	0.060852	0.476004	0.040*
C19	0.89945 (15)	0.12085 (7)	0.37742 (14)	0.0333 (4)
H19	0.948551	0.096015	0.338346	0.040*
C20	0.89502 (16)	0.17799 (7)	0.35160 (13)	0.0340 (4)
H20	0.940395	0.192231	0.294808	0.041*
C21	0.82428 (15)	0.21376 (6)	0.40907 (13)	0.0307 (3)
H21	0.821313	0.252776	0.391120	0.037*
C22	0.68432 (14)	0.23256 (6)	0.55928 (13)	0.0274 (3)
C23	0.62656 (15)	0.32838 (6)	0.60878 (13)	0.0287 (3)
H23A	0.645478	0.318990	0.691569	0.034*
H23B	0.528567	0.326108	0.580844	0.034*
C24	0.67452 (14)	0.38781 (6)	0.59184 (13)	0.0282 (3)
H24A	0.657057	0.396569	0.508767	0.034*
H24B	0.772454	0.389781	0.620334	0.034*
C25	0.60587 (14)	0.43202 (6)	0.65406 (13)	0.0281 (3)
H25A	0.507645	0.428610	0.628832	0.034*
H25B	0.627615	0.424548	0.737622	0.034*
C26	0.64836 (15)	0.49200 (6)	0.63151 (13)	0.0299 (3)
H26A	0.745500	0.495970	0.662168	0.036*
H26B	0.633617	0.498135	0.547542	0.036*
C27	0.57397 (15)	0.53755 (6)	0.68457 (13)	0.0290 (3)
H27A	0.476475	0.533037	0.656339	0.035*
H27B	0.591871	0.532805	0.768981	0.035*
C28	0.61575 (15)	0.59657 (6)	0.65560 (13)	0.0290 (3)
H28A	0.598270	0.601065	0.571136	0.035*
H28B	0.713278	0.600909	0.683886	0.035*
C29	0.54247 (14)	0.64293 (6)	0.70740 (13)	0.0276 (3)
H29A	0.444855	0.638456	0.679834	0.033*
H29B	0.560880	0.638857	0.791961	0.033*
C30	0.58368 (15)	0.70104 (7)	0.67682 (13)	0.0307 (3)

Atomic displacement parameters (Å²)

	U^{11}	U^{22}	U^{33}	U^{12}	U^{13}	U^{23}
O1	0.0545 (7)	0.0240 (6)	0.0518 (7)	−0.0004 (5)	0.0289 (6)	0.0014 (5)
O2	0.0444 (6)	0.0254 (6)	0.0342 (6)	0.0002 (4)	0.0203 (5)	−0.0001 (4)
O3	0.0623 (7)	0.0274 (6)	0.0501 (7)	0.0004 (5)	0.0380 (6)	0.0026 (5)
O4	0.0576 (7)	0.0215 (5)	0.0488 (7)	0.0014 (5)	0.0347 (6)	0.0007 (5)
O5	0.0504 (7)	0.0223 (6)	0.0422 (6)	0.0033 (5)	0.0244 (5)	0.0049 (5)
O6	0.0501 (6)	0.0223 (6)	0.0431 (6)	0.0005 (5)	0.0281 (5)	0.0019 (5)
O7	0.0615 (7)	0.0273 (6)	0.0541 (7)	−0.0002 (5)	0.0392 (6)	0.0013 (5)
O8	0.0531 (7)	0.0226 (6)	0.0438 (7)	−0.0003 (5)	0.0291 (5)	−0.0019 (5)
N1	0.0388 (7)	0.0232 (7)	0.0361 (7)	−0.0006 (5)	0.0191 (6)	−0.0017 (5)
N2	0.0375 (6)	0.0218 (6)	0.0312 (6)	0.0010 (5)	0.0173 (5)	0.0012 (5)
C1	0.0312 (7)	0.0246 (7)	0.0252 (7)	0.0009 (6)	0.0066 (6)	−0.0016 (6)
C2	0.0347 (7)	0.0263 (8)	0.0286 (7)	0.0000 (6)	0.0100 (6)	0.0004 (6)
C3	0.0467 (9)	0.0220 (8)	0.0426 (9)	0.0022 (6)	0.0135 (7)	−0.0023 (7)
C4	0.0423 (8)	0.0311 (9)	0.0392 (9)	0.0052 (7)	0.0168 (7)	−0.0051 (7)
C5	0.0423 (8)	0.0340 (9)	0.0376 (9)	0.0008 (7)	0.0201 (7)	−0.0011 (7)
C6	0.0402 (8)	0.0254 (8)	0.0329 (8)	−0.0002 (6)	0.0140 (6)	−0.0004 (6)
C7	0.0321 (7)	0.0244 (7)	0.0262 (7)	−0.0009 (6)	0.0084 (6)	−0.0005 (6)
C8	0.0403 (8)	0.0232 (8)	0.0406 (9)	0.0012 (6)	0.0201 (7)	−0.0034 (6)
C9	0.0393 (8)	0.0243 (8)	0.0387 (9)	0.0010 (6)	0.0187 (7)	−0.0004 (6)
C10	0.0353 (8)	0.0231 (8)	0.0358 (8)	0.0003 (6)	0.0142 (6)	−0.0012 (6)
C11	0.0364 (7)	0.0238 (8)	0.0327 (8)	0.0014 (6)	0.0138 (6)	−0.0008 (6)
C12	0.0346 (7)	0.0249 (8)	0.0320 (8)	−0.0001 (6)	0.0138 (6)	−0.0019 (6)
C13	0.0386 (8)	0.0237 (8)	0.0353 (8)	0.0005 (6)	0.0178 (6)	−0.0007 (6)
C14	0.0383 (8)	0.0235 (7)	0.0300 (8)	−0.0004 (6)	0.0155 (6)	−0.0021 (6)
C15	0.0413 (8)	0.0262 (8)	0.0333 (8)	0.0012 (6)	0.0173 (6)	0.0009 (6)
C16	0.0323 (7)	0.0239 (8)	0.0271 (7)	0.0003 (6)	0.0095 (6)	−0.0011 (6)
C17	0.0344 (7)	0.0248 (8)	0.0300 (8)	−0.0001 (6)	0.0102 (6)	0.0013 (6)
C18	0.0409 (8)	0.0228 (8)	0.0369 (8)	0.0024 (6)	0.0109 (7)	−0.0012 (6)
C19	0.0397 (8)	0.0303 (8)	0.0327 (8)	0.0036 (6)	0.0136 (6)	−0.0067 (6)
C20	0.0443 (8)	0.0327 (9)	0.0293 (8)	0.0008 (7)	0.0177 (7)	0.0000 (6)
C21	0.0411 (8)	0.0222 (7)	0.0318 (8)	0.0010 (6)	0.0142 (6)	0.0014 (6)
C22	0.0338 (7)	0.0222 (7)	0.0281 (7)	0.0004 (6)	0.0108 (6)	0.0011 (6)
C23	0.0360 (7)	0.0227 (7)	0.0312 (8)	0.0021 (6)	0.0162 (6)	−0.0003 (6)
C24	0.0333 (7)	0.0234 (7)	0.0302 (7)	0.0015 (6)	0.0120 (6)	0.0003 (6)
C25	0.0342 (7)	0.0232 (7)	0.0299 (7)	0.0018 (6)	0.0133 (6)	−0.0002 (6)
C26	0.0359 (7)	0.0229 (7)	0.0339 (8)	0.0012 (6)	0.0142 (6)	−0.0006 (6)
C27	0.0354 (7)	0.0228 (8)	0.0312 (8)	0.0005 (6)	0.0119 (6)	−0.0028 (6)
C28	0.0359 (7)	0.0231 (8)	0.0305 (7)	0.0010 (6)	0.0129 (6)	0.0003 (6)
C29	0.0335 (7)	0.0243 (7)	0.0274 (7)	0.0005 (6)	0.0116 (6)	−0.0014 (6)
C30	0.0371 (8)	0.0251 (8)	0.0325 (8)	−0.0007 (6)	0.0135 (6)	−0.0003 (6)

Geometric parameters (Å, º)

O1—H1	0.89 (2)	C12—H12A	0.9900
O1—C2	1.3561 (18)	C12—H12B	0.9900

O2—C7	1.2599 (17)	C12—C13	1.518 (2)
O3—C15	1.2114 (18)	C13—H13A	0.9900
O4—H4	0.93 (2)	C13—H13B	0.9900
O4—C15	1.3318 (18)	C13—C14	1.525 (2)
O5—H5A	0.87 (2)	C14—H14A	0.9900
O5—C17	1.3561 (18)	C14—H14B	0.9900
O6—C22	1.2598 (18)	C14—C15	1.504 (2)
O7—C30	1.2115 (18)	C16—C17	1.410 (2)
O8—H8	0.94 (2)	C16—C21	1.401 (2)
O8—C30	1.3295 (18)	C16—C22	1.4872 (19)
N1—H1A	0.887 (19)	C17—C18	1.393 (2)
N1—C7	1.325 (2)	C18—H18	0.9500
N1—C8	1.4619 (19)	C18—C19	1.376 (2)
N2—H2	0.905 (19)	C19—H19	0.9500
N2—C22	1.3279 (19)	C19—C20	1.390 (2)
N2—C23	1.4645 (18)	C20—H20	0.9500
C1—C2	1.406 (2)	C20—C21	1.377 (2)
C1—C6	1.405 (2)	C21—H21	0.9500
C1—C7	1.486 (2)	C23—H23A	0.9900
C2—C3	1.393 (2)	C23—H23B	0.9900
C3—H3	0.9500	C23—C24	1.520 (2)
C3—C4	1.377 (2)	C24—H24A	0.9900
C4—H4A	0.9500	C24—H24B	0.9900
C4—C5	1.386 (2)	C24—C25	1.5283 (19)
C5—H5	0.9500	C25—H25A	0.9900
C5—C6	1.374 (2)	C25—H25B	0.9900
C6—H6	0.9500	C25—C26	1.527 (2)
C8—H8A	0.9900	C26—H26A	0.9900
C8—H8B	0.9900	C26—H26B	0.9900
C8—C9	1.520 (2)	C26—C27	1.5247 (19)
C9—H9A	0.9900	C27—H27A	0.9900
C9—H9B	0.9900	C27—H27B	0.9900
C9—C10	1.523 (2)	C27—C28	1.523 (2)
C10—H10A	0.9900	C28—H28A	0.9900
C10—H10B	0.9900	C28—H28B	0.9900
C10—C11	1.524 (2)	C28—C29	1.5245 (19)
C11—H11A	0.9900	C29—H29A	0.9900
C11—H11B	0.9900	C29—H29B	0.9900
C11—C12	1.5268 (19)	C29—C30	1.507 (2)

C2—O1—H1	105.5 (14)	C15—C14—H14A	109.1
C15—O4—H4	111.5 (13)	C15—C14—H14B	109.1
C17—O5—H5A	104.0 (13)	O3—C15—O4	119.66 (14)
C30—O8—H8	110.5 (13)	O3—C15—C14	122.73 (14)
C7—N1—H1A	121.8 (12)	O4—C15—C14	117.61 (12)
C7—N1—C8	123.00 (13)	C17—C16—C22	119.75 (13)
C8—N1—H1A	115.2 (12)	C21—C16—C17	118.10 (13)
C22—N2—H2	122.3 (12)	C21—C16—C22	122.12 (13)

C22—N2—C23	122.59 (12)	O5—C17—C16	122.69 (13)
C23—N2—H2	115.1 (12)	O5—C17—C18	117.38 (14)
C2—C1—C7	120.21 (13)	C18—C17—C16	119.93 (14)
C6—C1—C2	117.99 (13)	C17—C18—H18	119.8
C6—C1—C7	121.75 (13)	C19—C18—C17	120.43 (14)
O1—C2—C1	122.61 (13)	C19—C18—H18	119.8
O1—C2—C3	117.24 (14)	C18—C19—H19	119.7
C3—C2—C1	120.15 (14)	C18—C19—C20	120.51 (14)
C2—C3—H3	120.0	C20—C19—H19	119.7
C4—C3—C2	120.08 (15)	C19—C20—H20	120.3
C4—C3—H3	120.0	C21—C20—C19	119.40 (14)
C3—C4—H4A	119.6	C21—C20—H20	120.3
C3—C4—C5	120.83 (14)	C16—C21—H21	119.2
C5—C4—H4A	119.6	C20—C21—C16	121.63 (14)
C4—C5—H5	120.3	C20—C21—H21	119.2
C6—C5—C4	119.36 (15)	O6—C22—N2	120.77 (13)
C6—C5—H5	120.3	O6—C22—C16	119.77 (13)
C1—C6—H6	119.2	N2—C22—C16	119.46 (13)
C5—C6—C1	121.60 (15)	N2—C23—H23A	109.6
C5—C6—H6	119.2	N2—C23—H23B	109.6
O2—C7—N1	121.20 (13)	N2—C23—C24	110.47 (11)
O2—C7—C1	119.73 (13)	H23A—C23—H23B	108.1
N1—C7—C1	119.04 (13)	C24—C23—H23A	109.6
N1—C8—H8A	109.7	C24—C23—H23B	109.6
N1—C8—H8B	109.7	C23—C24—H24A	109.1
N1—C8—C9	109.82 (12)	C23—C24—H24B	109.1
H8A—C8—H8B	108.2	C23—C24—C25	112.69 (11)
C9—C8—H8A	109.7	H24A—C24—H24B	107.8
C9—C8—H8B	109.7	C25—C24—H24A	109.1
C8—C9—H9A	109.1	C25—C24—H24B	109.1
C8—C9—H9B	109.1	C24—C25—H25A	109.1
C8—C9—C10	112.56 (12)	C24—C25—H25B	109.1
H9A—C9—H9B	107.8	H25A—C25—H25B	107.8
C10—C9—H9A	109.1	C26—C25—C24	112.62 (12)
C10—C9—H9B	109.1	C26—C25—H25A	109.1
C9—C10—H10A	109.0	C26—C25—H25B	109.1
C9—C10—H10B	109.0	C25—C26—H26A	108.7
C9—C10—C11	112.95 (12)	C25—C26—H26B	108.7
H10A—C10—H10B	107.8	H26A—C26—H26B	107.6
C11—C10—H10A	109.0	C27—C26—C25	114.17 (12)
C11—C10—H10B	109.0	C27—C26—H26A	108.7
C10—C11—H11A	108.9	C27—C26—H26B	108.7
C10—C11—H11B	108.9	C26—C27—H27A	109.2
C10—C11—C12	113.22 (12)	C26—C27—H27B	109.2
H11A—C11—H11B	107.7	H27A—C27—H27B	107.9
C12—C11—H11A	108.9	C28—C27—C26	112.16 (12)
C12—C11—H11B	108.9	C28—C27—H27A	109.2
C11—C12—H12A	109.0	C28—C27—H27B	109.2

C11—C12—H12B	109.0	C27—C28—H28A	108.9
H12A—C12—H12B	107.8	C27—C28—H28B	108.9
C13—C12—C11	112.88 (12)	C27—C28—C29	113.21 (12)
C13—C12—H12A	109.0	H28A—C28—H28B	107.8
C13—C12—H12B	109.0	C29—C28—H28A	108.9
C12—C13—H13A	109.0	C29—C28—H28B	108.9
C12—C13—H13B	109.0	C28—C29—H29A	109.1
C12—C13—C14	112.81 (12)	C28—C29—H29B	109.1
H13A—C13—H13B	107.8	H29A—C29—H29B	107.8
C14—C13—H13A	109.0	C30—C29—C28	112.57 (12)
C14—C13—H13B	109.0	C30—C29—H29A	109.1
C13—C14—H14A	109.1	C30—C29—H29B	109.1
C13—C14—H14B	109.1	O7—C30—O8	119.37 (14)
H14A—C14—H14B	107.8	O7—C30—C29	122.98 (14)
C15—C14—C13	112.48 (12)	O8—C30—C29	117.64 (12)

O1—C2—C3—C4	−179.89 (15)	C13—C14—C15—O3	−7.0 (2)
O5—C17—C18—C19	−179.62 (14)	C13—C14—C15—O4	173.25 (14)
N1—C8—C9—C10	−177.24 (13)	C16—C17—C18—C19	−0.6 (2)
N2—C23—C24—C25	179.24 (12)	C17—C16—C21—C20	−0.8 (2)
C1—C2—C3—C4	0.3 (2)	C17—C16—C22—O6	−7.3 (2)
C2—C1—C6—C5	0.0 (2)	C17—C16—C22—N2	171.86 (14)
C2—C1—C7—O2	−3.7 (2)	C17—C18—C19—C20	−0.1 (2)
C2—C1—C7—N1	178.26 (14)	C18—C19—C20—C21	0.4 (2)
C2—C3—C4—C5	0.3 (3)	C19—C20—C21—C16	0.1 (2)
C3—C4—C5—C6	−0.8 (3)	C21—C16—C17—O5	−179.98 (14)
C4—C5—C6—C1	0.6 (2)	C21—C16—C17—C18	1.0 (2)
C6—C1—C2—O1	179.78 (14)	C21—C16—C22—O6	174.37 (14)
C6—C1—C2—C3	−0.5 (2)	C21—C16—C22—N2	−6.5 (2)
C6—C1—C7—O2	173.61 (14)	C22—N2—C23—C24	170.46 (14)
C6—C1—C7—N1	−4.4 (2)	C22—C16—C17—O5	1.6 (2)
C7—N1—C8—C9	−172.40 (14)	C22—C16—C17—C18	−177.34 (14)
C7—C1—C2—O1	−2.8 (2)	C22—C16—C21—C20	177.53 (14)
C7—C1—C2—C3	176.95 (14)	C23—N2—C22—O6	−0.4 (2)
C7—C1—C6—C5	−177.40 (15)	C23—N2—C22—C16	−179.57 (13)
C8—N1—C7—O2	−0.3 (2)	C23—C24—C25—C26	−176.79 (13)
C8—N1—C7—C1	177.71 (13)	C24—C25—C26—C27	175.49 (13)
C8—C9—C10—C11	179.41 (13)	C25—C26—C27—C28	−177.66 (13)
C9—C10—C11—C12	−178.64 (13)	C26—C27—C28—C29	179.84 (12)
C10—C11—C12—C13	−179.03 (13)	C27—C28—C29—C30	−179.31 (13)
C11—C12—C13—C14	−177.60 (13)	C28—C29—C30—O7	6.1 (2)
C12—C13—C14—C15	178.05 (13)	C28—C29—C30—O8	−174.35 (13)

Hydrogen-bond geometry (Å, º)

D—H···*A*	*D*—H	H···*A*	*D*···*A*	*D*—H···*A*
O1—H1···O2	0.89 (2)	1.76 (2)	2.5737 (16)	151 (2)
O4—H4···O2^{i}	0.93 (2)	1.73 (2)	2.6637 (15)	177 (2)

O5—H5*A*···O6	0.87 (2)	1.76 (2)	2.5660 (15)	153.1 (19)
O8—H8···O6^{ii}	0.94 (2)	1.71 (2)	2.6479 (15)	176.4 (19)
N1—H1*A*···O7	0.887 (19)	2.15 (2)	3.0220 (17)	169.3 (17)
N2—H2···O3	0.905 (19)	2.078 (19)	2.9708 (17)	168.6 (16)

Symmetry codes: (i) −*x*+2, *y*−1/2, −*z*+1/2; (ii) −*x*+1, *y*+1/2, −*z*+3/2.